ARCHIVE OF MECHANICAL ENGINEERING

DOI: 10.24425/ame.2026.12693 Early Access; pp. 1–28

Ming QIU [1], Jian XIONG [1], Jie SONG [1], Jie ZHOU [2], Lin-Tao WANG [1]

Gas-guided rotary-valve shared-nozzle rear-jet device for recoil suppression of high-rate-of-fire rotary-barrel weapons

Received 26 May 2026, **Revised** 19 August 2026, **Accepted** 8 September 2026, **Published online** 19 November 2026

Keywords: rotary barrel weapon, gas-guided rotary valve, shared rear-jet nozzle, two-phase flow, interior ballistics, recoil reduction

High-rate-of-fire rotary-barrel weapons suffer from severe recoil force accumulation during sustained firing, which poses significant challenges for their integration onto lightweight, rapidly moving platforms such as aircraft and light vehicles. To address this issue, a gas-guided rotary-valve-based shared-nozzle rear-jet control device is proposed. This study investigates the feasibility of synchronized rear-jet operation and its effects on in-bore propellant gas dynamics through numerical simulation. For a 14.5 mm three-barrel rotary weapon, a front-mounted self-locking three-in-one gas diversion device and a rear-mounted rotary valve shared-nozzle system were designed. Incorporating the gas-solid coupled dynamics of the rotary valve, a two-phase interior ballistic model was established. The coupled system of partial differential, ordinary differential, and algebraic equations was solved using the MacCormack finite-difference scheme and Runge–Kutta methods. Under the present modeling conditions and the selected nominal parameters, the numerical results predict that the recoil reduction efficiency reaches 46.85% over one firing cycle at 3000 rounds/min while limiting muzzle velocity reduction to only 0.85% (from 960.42 m/s to 952.29 m/s). This study provides a preliminary numerical framework and design insight for synchronized shared-nozzle rear-jet control in rotary-barrel weapons.

✉ Jian XIONG, e-mail: xiongjian@njust.edu.cn

[1]School of Mechanical Engineering, Nanjing University of Science and Technology, Nanjing, People's Republic of China

[2]School of Chemistry and Chemical Engineering, Nanjing University of Science and Technology, Nanjing, People's Republic of China



© 2026. The Author(s). This is an open-access article distributed under the terms of the Creative Commons Attribution (CC-BY 4.0, https://creativecommons.org/licenses/by/4.0/), which permits use, distribution, and reproduction in any medium, provided that the author and source are cited.

1. Introduction

Rotary barrel weapons provide substantially higher firing rates and greater firepower than conventional single-barrel systems. However, their inability to reset between shots during continuous firing results in severe superposition of recoil forces. This not only restricts platform compatibility but also imposes intense impact loads on the mounting structure [1]. The resulting vibrations significantly hinder the deployment of these weapons on rapidly moving platforms, such as aircraft, light vehicles, and naval vessels. Consequently, effective recoil reduction during sustained high-rate fire has become an urgent requirement.

Current recoil mitigation technologies can be broadly classified into structural and internal-energy-based approaches. Structural methods include soft recoil systems [2] and magnetorheological fluid dampers [3, 4]. For example, Liu et al. [5] optimized the buffer parameters of a counter-recoil mechanism for rotary barrel weapons, successfully preventing recoil force accumulation. Nevertheless, these approaches typically require additional space and mass, which limits their applicability to lightweight platforms.

Internal-energy-based methods harness the residual energy carried by propellant gases discharged from the muzzle, which would otherwise not be effectively utilized for projectile acceleration. The energy carried by the discharged propellant gases can exceed 40% of the total chemical energy released by propellant combustion. A classic example is the muzzle brake, which redirects gas rearward to generate a counterforce. However, it activates only after the projectile exits the muzzle. With structural improvements and optimizations, its recoil reduction efficiency can exceed 40% [6–8].

Liao [9] proposed a rearward-jet technique that vents propellant gas through side-wall ports in the barrel. Although effective in reducing recoil impulse, this method causes an abrupt drop in projectile base pressure once the projectile passes the ports, inevitably leading to muzzle velocity loss. In the configuration investigated by Liao [9], a recoil-impulse reduction of approximately 35% was accompanied by a muzzle-velocity reduction of approximately 7%. Li et al. [10] further explored rear-jet recoil reduction for large-caliber rotary barrel weapons, confirming the feasibility of internal-energy-based approaches. However, considerable muzzle velocity loss remained an issue. Han [11] developed a piston-crankshaft-based rear-jet control device for rotary barrel weapons; yet, in practice, the crankshaft exhibits oscillatory "drive–brake–reverse" motion. This prevents the exhaust ports from remaining fully open, resulting in insufficient rearward gas discharge.

For single-barrel weapons, researchers have made considerable efforts to preserve the recoil-reduction benefits of internal-energy-based methods while minimizing muzzle velocity loss. Si [12] proposed a piston-controlled lateral rear-jet device, while Qiu [13] developed a gas-operated rear-jet system. Both designs effectively mitigate the adverse effects of rarefaction waves on muzzle velocity.

However, directly replicating these single-barrel devices across every barrel of a rotary barrel weapon would substantially increase structural complexity, rotational inertia, and drive system load, thereby reducing overall efficiency. Consequently, developing a compact shared rear-jet control device tailored for rotary barrel assemblies remains a critical challenge. Such a device must achieve precise exhaust synchronization with the firing barrel, minimize rarefaction wave effects on muzzle velocity, and prevent high-pressure gas leakage into non-firing barrels.

To address these issues, this study proposes a gas-guided rotary valve mechanism (GRV). By utilizing propellant gas to drive a rotary valve, the device enables synchronized rearward gas discharge from the firing barrel through a common shared nozzle. This design aims to reduce recoil impulse while minimizing the associated loss of muzzle velocity.

Assessing the performance of this coupled gas-operated mechanism requires an interior-ballistics model that can describe transient gas-solid interaction, gas diversion, valve motion, and nozzle discharge. Two-phase flow interior ballistic theory has been widely adopted in gun launch simulations [14–19]. For example, Monreal [20] established a one-dimensional two-phase model for artillery systems based on porous propellant combustion characteristics, while Menshov [21] employed a two-dimensional axisymmetric model to investigate combustion under non-uniform propellant distribution. Building upon this established theoretical framework, the present study fully incorporates the gas-solid coupled dynamics of the gas-operated system, including the movable obturator blocks, rotary valve, and locking pin. A comprehensive one-dimensional two-phase flow interior ballistic model for the proposed rotary barrel weapon is developed and numerically solved. The effects of the rotary valve on in-bore flow characteristics, projectile muzzle velocity, and overall recoil reduction performance are systematically investigated. This study aims to provide a robust analytical framework and reference for synchronized common-nozzle rear-jet control in rotary barrel weapons using rotary valve mechanisms.

2. Principle of the GRV-equipped rotary barrel weapon

Fig. 1 shows a schematic diagram of the proposed gas-guided rotary valve rotary barrel weapon (GRV-equipped rotary barrel weapon), which illustrates two different states. The main components include the front and rear barrel clamps, movable sealing blocks, rotating piston, one-way valve, locking pin, exhaust rotor, and shared rear-jet nozzle. As shown in Fig. 2, a front-mounted self-locking three-in-one gas diversion triggering device, consisting of three movable sealing blocks, is installed within the front barrel clamp. This device directs high-pressure propellant gas from the gas channel of the firing barrel into the high-pressure chamber while effectively preventing leakage into the non-firing barrels. The rotary valve assembly, which comprises the rotating piston, connecting rod, and exhaust rotor, is mounted in the rear barrel clamp, with the shared rear-jet nozzle positioned directly behind

the exhaust rotor. Detailed internal structures of the recoil-reduction device along the central axis of the barrel assembly are illustrated in Figs. 1–5. Arrows A, B, and C in figs indicate propellant gas flowing into the lateral gas channel, entering the rotating piston through the gas-transfer tube to actuate the valve, and entering the shared nozzle through the rear exhaust port, respectively.

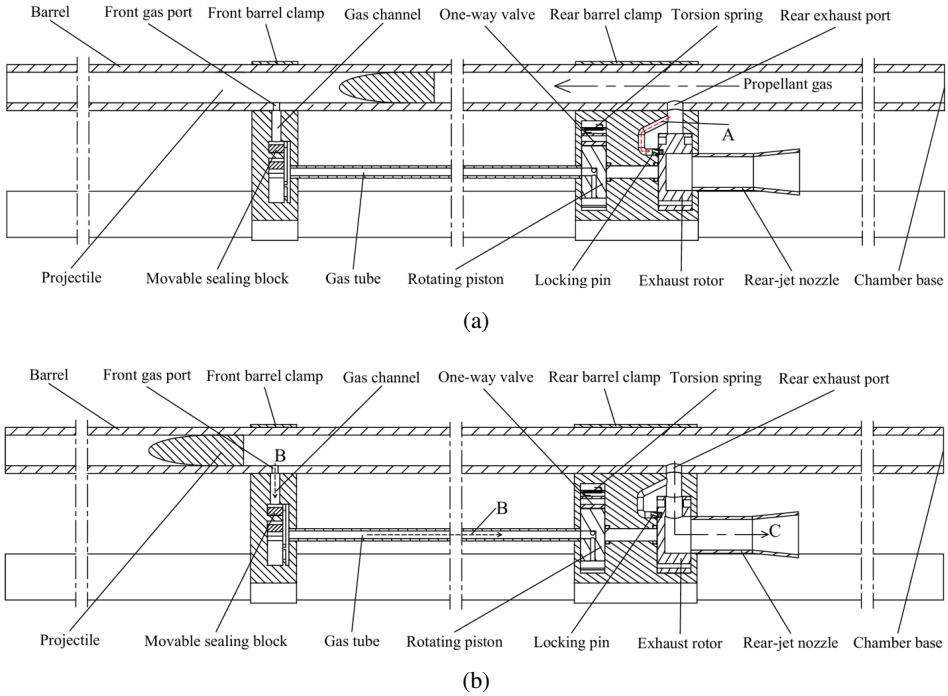


Fig. 1. Schematic of the GRV-equipped rotary barrel weapon. (a) Exhaust passage closed. (b) Exhaust passage fully open

During continuous firing, the barrels of the rotary weapon fire sequentially at a fixed angular position, with only one barrel actively firing while the others remain in the ready-to-fire state. The operating cycle of the GRV system can be divided into five distinct stages:

1. Triggering stage: As the projectile travels down the bore, it first passes the rear exhaust port, allowing a small amount of propellant gas to enter the lateral gas channel. This gas drives the locking pin outward against the spring force. At this stage, the exhaust channel remains closed, preventing premature gas discharge through the rear-jet nozzle, as shown in Fig. 1a. Consequently, most of the propellant gas continues to accelerate the projectile forward.
2. Driving stage: After the projectile passes the front gas port, high-pressure propellant gas flows into the gas-transfer channel of the front barrel clamp. This drives the gas diversion device to its limit position, as shown in Fig. 2.

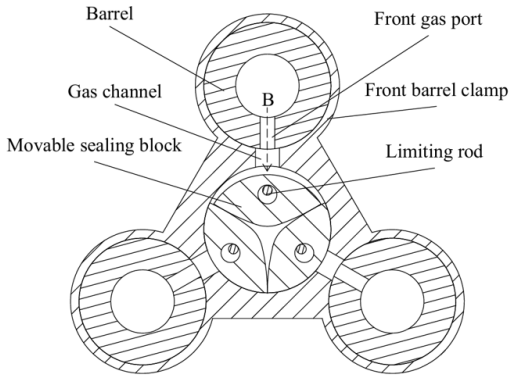


Fig. 2. Schematic of the front-mounted self-locking three-in-one gas diversion device at its limit position

The gas is then directed into the high-pressure chamber, where it actuates the rotary valve assembly to rotate.

3. Positioning stage: When the exhaust rotor reaches the predetermined angular position, the locking pin – already extended by the propellant gas pressure – engages with the locking hole on the exhaust rotor. This ensures precise alignment between the exhaust channel and the rotor exhaust port, thereby achieving accurate positioning, as shown in Fig. 4b.
4. Exhaust stage: Once the exhaust channel is fully opened, a large volume of propellant gas is discharged rearward at high velocity through the common rear-jet nozzle. The resulting forward reaction thrust effectively reduces the recoil impulse during firing, as shown in Fig. 1b.
5. Reset stage: After firing is completed, the locking pin returns to its initial position under the action of the return spring. This prevents interference with the rotary valve during subsequent firing cycles and ensures reliable continuous operation of the device at high firing rates.

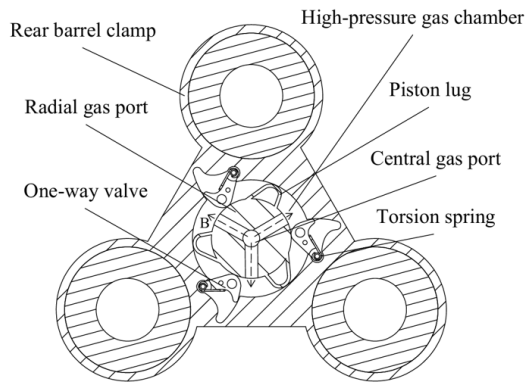


Fig. 3. Initial installation position of the rotating piston

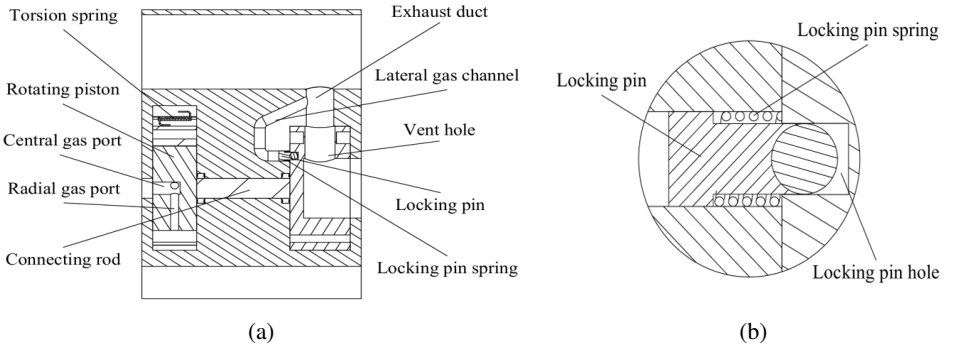


Fig. 4. Assembly drawing of internal components in the rear barrel clamp. (a) Internal components in the rear barrel clamp, (b) Enlarged partial view of the locking pin area

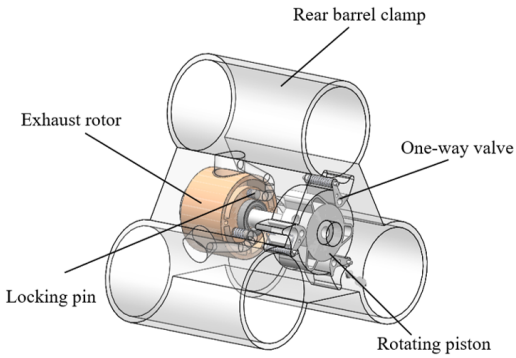


Fig. 5. Schematic of the rotary valve

3. The firing process model of GRV-equipped rotary barrel weapon

3.1. Fundamental assumptions

The propellant gas flow inside the chamber, lateral gas channels, gas-transfer channels, and rear-jet nozzle during the firing process of a GRV-equipped rotary barrel weapon is highly complex owing to its two-phase nature. To develop a mathematical model that achieves a reasonable balance between accuracy and computational efficiency, the following assumptions are adopted. These assumptions have been widely adopted in theoretical studies and the numerical calculations of internal ballistics for weapons [13, 21–24]:

1. The propellant grains are treated as a pseudo-fluid with continuous-medium properties.
2. The propellant gas flow in the bore, lateral gas channels, gas-transfer channels, and rear-jet nozzle is assumed to be one-dimensional and unsteady.
3. During an individual firing event, only the barrel at the firing position is connected to the shared rear-jet flow path through the GRV-controlled gas-guidance

and sealing arrangement. Therefore, the in-bore flow of the active barrel is modeled as an independent single-barrel system during its own firing event.
4. Propellant combustion follows the geometric burning law and the exponential burning-rate law. All propellant grains are assumed to be identical in geometry and size, with constant and incompressible density.
5. Viscous dissipation and heat transfer to the barrel wall are neglected.
6. Gas flow through branched or curved passages is treated as isentropic.
7. Only the rarefaction waves generated at the rear exhaust port are considered in the numerical simulation; rarefaction waves originating from other locations within the bore are neglected.

3.2. Governing equations of the two-phase flow model in the barrel

The governing equations for the two-phase flow model comprise the mass and momentum conservation equations for both the gas and solid phases, together with the energy conservation equation for the gas phase [24]. Compared with a conventional rotary-barrel weapon, the proposed GRV-equipped configuration involves additional transient gas-transfer processes when the projectile uncovers the rear exhaust port and the front gas port, and when the rear-jet passage subsequently opens. Accordingly, the conservation equations, including the source terms representing these gas-transfer processes, can be expressed in the following vector form [22, 23]:

$$\frac{\partial \boldsymbol{U}}{\partial t}+\frac{\partial \boldsymbol{F}}{\partial x}=\begin{cases}\boldsymbol{H} & \text{Before the projectile reaches the rear exhaust port,}\\ \boldsymbol{H}-\boldsymbol{L} & \text{After the projectile passes the rear exhaust port,}\\ \boldsymbol{H}-\boldsymbol{L}-\boldsymbol{J} & \text{After the projectile passes the front gas port,}\\ \boldsymbol{H}-\boldsymbol{J}-\boldsymbol{K} & \text{After the rear exhaust port of the barrel opens,}\end{cases} \tag{1}$$

$$\boldsymbol{U}=\begin{bmatrix} A\varphi\rho_g \\ A(1-\varphi)\rho_p \\ A\varphi\rho_g u_g \\ A(1-\varphi)\rho_p u_p \\ A\varphi\rho_g\left(e_g+\dfrac{u_g^2}{2}\right)\end{bmatrix}, \tag{2}$$

$$\boldsymbol{F}=\begin{bmatrix} A\varphi\rho_g u_g \\ A(1-\varphi)\rho_p u_p \\ A\varphi\rho_g\left(u_g^2+\dfrac{p}{\rho_g}\right) \\ A(1-\varphi)\left(\rho_p u_p^2+p+\tau_p\right) \\ A\varphi\rho_g u_g\left(e_g+\dfrac{u_g^2}{2}+\dfrac{p}{\rho_g}\right)\end{bmatrix}, \tag{3}$$

$$\boldsymbol{H}=\begin{bmatrix} A(\dot{m}_c+\dot{m}_{ign}) \\ -A\dot{m}_c \\ A(\dot{m}_c u_p+\dot{m}_{ign}u_{ign}-f_s)+p\dfrac{\partial A\varphi}{\partial x} \\ A(f_s-\dot{m}_c u_p)+p\dfrac{\partial A(1-\varphi)}{\partial x}+\tau_p(1-\varphi)\dfrac{\partial A}{\partial x} \\ A\left(\dot{m}_c\left(e_p+\dfrac{p}{\rho_p}+\dfrac{u_p^2}{2}\right)+\dot{m}_{ign}H_{ign}-f_s u_p-Q_s\right)-p\dfrac{\partial A\varphi}{\partial x} \end{bmatrix}, \tag{4}$$

$$\boldsymbol{L}=\begin{bmatrix} A\dot{m}_{gc} \\ A\dot{m}_{pc} \\ A\dot{m}_{gc}u_{gc} \\ A\dot{m}_{pc}u_{pc} \\ A\dot{m}_{gc}\left(e_{gc}+\dfrac{p_c}{\rho_{gc}}+\dfrac{u_{gc}^2}{2}\right) \end{bmatrix}, \tag{5}$$

$$\boldsymbol{J}=\begin{bmatrix} A\dot{m}_{gb} \\ 0 \\ A\dot{m}_{gb}u_{gb} \\ 0 \\ A\dot{m}_{gb}\left(e_{gb}+\dfrac{p_b}{\rho_{gb}}+\dfrac{u_{gb}^2}{2}\right) \end{bmatrix}, \tag{6}$$

$$\boldsymbol{K}=\begin{bmatrix} A\dot{m}_{gr} \\ A\dot{m}_{pr} \\ A\dot{m}_{gr}u_{gr} \\ A\dot{m}_{pr}u_{pr} \\ A\dot{m}_{gr}\left(e_{gr}+\dfrac{p_r}{\rho_{gr}}+\dfrac{u_{gr}^2}{2}\right) \end{bmatrix}. \tag{7}$$

In the mathematical model, the terms $\boldsymbol{L}$, $\boldsymbol{J}$, $\boldsymbol{K}$ represent the flow exchange between the bore and the lateral gas channel, gas-transfer channel and the rear-jet nozzle, respectively. Where A is the cross-sectional area of the barrel bore; p is the pressure in the barrel; φ is the porosity; f_s is the interphase drag force; τ_p is the interparticle stress; Q_s is the interphase heat transfer rate; ρ_g and ρ_p are the densities of the gas and solid phases, respectively; u_g and u_p are the velocities of the gas and solid phases, respectively; u_{ign} and H_{ign} are the injection velocity of the primer gas and the gas-generation rate of the igniter, respectively; e_g and e_p are the specific internal energies of the gas and solid phases, respectively; $\dot{m}_{gc}$ and $\dot{m}_{\mathrm{pc}}$ are the volumetric mass flow rates of the gas and solid phases from the barrel into

the exhaust channel, respectively; u_{gc} and u_{pc} are the gas-phase and solid-phase velocities at the rear exhaust port, respectively; e_{gc} is the specific internal energy of the gas phase at the rear exhaust port; ρ_{gc} is the gas-phase density at the rear exhaust port; p_c is the pressure at the rear exhaust port; $\dot{m}_{gr}$ and $\dot{m}_{pr}$ are the volumetric mass flow rates of the gas phase and the solid phase flowing out from the rear nozzle, respectively; $\dot{m}_{gb}$ is the mass flow rate of the gas phase flowing out from the gas port; u_{gr} and u_{gb} are the gas-phase velocity at the rear exhaust port and the front gas port respectively. All other parameters are defined following the same convention. The corresponding values are listed in Table 2.

The equations needed to close the above governing equations, such as propellant combustion, interphase drag, and the two-phase flow in the rear-jet nozzle can be found in Ref. [8, 24].

3.3. Mathematical model of the rotary valve drive system

The gas parameters in the high-pressure chamber are described using mass and energy conservation equations [8]. The resulting chamber pressure is then coupled with the rotary valve motion model. To establish a numerically solvable motion model for the rotary piston, the following supplementary assumptions are introduced in addition to the basic assumptions presented in Section 3.1 [9, 10]:

1. Within the high-pressure chamber, spatial variations in gas-flow parameters are neglected. The gas pressure, density, and temperature are therefore represented by their spatially averaged values.
2. The gas in the high-pressure chamber is assumed to obey the ideal gas equation of state.
3. Leakage flow through the clearance between the high-pressure chamber and the rotating piston is treated as choked flow.

The mass conservation equation and the mass calculation formula for the gas inside the high pressure chamber are as follows:

$$\frac{dm_q}{dt} = q_{mb} - q_{mq}\,, \tag{8}$$

$$m_q = \rho_q V_q = \rho_q \left(V_{q0} + \frac{\pi}{120} l_1 \left(r_1^2 - r_2^2\right) \theta\right). \tag{9}$$

Taking the derivative of Eq. (9) and combining it with Eq. (8), the variation function of gas density in the high-pressure chamber can be derived, as shown in Eq. (10).

$$\frac{d\rho_q}{dt} = \frac{q_{mb} - q_{mq} - \frac{\pi}{120} l_1 \left(r_1^2 - r_2^2\right) \rho_q \omega}{\left(V_{q0} + \frac{\pi}{120} l_1 \left(r_1^2 - r_2^2\right) \theta\right)}\,. \tag{10}$$

In the above equations, q_{mb} and q_{mq} denote the mass flow rates of gas entering and exiting the high-pressure chamber, respectively; ρ_q is the gas density inside

the high-pressure chamber; V_{q0} is the initial volume of the high-pressure chamber; r_1, r_2, and l_1 represent the outer radius of the piston lug, the radius of the rotating piston, and the width of the piston lug, respectively; and θ and ω are the rotation angle and angular velocity of the rotating piston, respectively.

Based on the energy conservation equation for the gas inside the high-pressure chamber, the corresponding formulas are as follows [8]:

$$\frac{-\delta Q}{dt} + e_i q_{mb} - e_q q_{mq} = \frac{dU}{dt} + \frac{\delta A}{dt}, \tag{11}$$

$$\frac{\delta A}{dt} = \frac{p_q dV_q}{dt} = \frac{\pi}{120}\left(r_1^2 - r_2^2\right) l_1 p_q \omega, \tag{12}$$

$$\begin{aligned}\frac{dU}{dt} &= \frac{d}{dt}\left(\rho_q V_q C_v T_q\right) = \frac{d}{dt}\left(\frac{p_q V_q}{\gamma - 1}\right) \\ &= \frac{1}{\gamma - 1}\left(V_q \frac{dp_q}{dt} + \frac{\pi}{120} p_q \left(r_1^2 - r_2^2\right) l_1 \omega\right),\end{aligned} \tag{13}$$

$$\begin{aligned}\frac{\delta Q}{dt} &= h\left(T_q - T_c\right) F_q \\ &= h\left(T_q - T_c\right)\left(F_{q0} + \frac{\pi}{60}\left(r_1^2 - r_2^2\right)\theta + \frac{\pi}{60} l_1 \left(r_1 + r_2\right)\theta\right).\end{aligned} \tag{14}$$

Combining Eqs. (11) through (14) yields the expression for the gas pressure inside the high-pressure chamber as:

$$\begin{aligned}\frac{dp_q}{dt} = &\frac{\gamma - 1}{V_{q0} + \frac{\pi}{120} l_1 \left(r_1^2 - r_2^2\right)\theta} \\ &\cdot \left(-\frac{\delta Q}{dt} + e_i q_{mb} - e_q q_{mq} - \frac{\pi}{120}\frac{\gamma}{\gamma - 1} l_1 \left(r_1^2 - r_2^2\right) p_q \omega\right),\end{aligned} \tag{15}$$

where δQ, dU, and δA denote the infinitesimal heat transfer, change in internal energy, and infinitesimal work done by the system on the surroundings, respectively; Q and F_{q0} represent the heat loss and the initial heat dissipation area of the high-pressure chamber, respectively; γ, e_i and e_q are the specific heat ratio, and the specific internal energies of the gas entering and exiting the high-pressure chamber, respectively.

Considering that the energy of the gas flowing into and out of the high-pressure chamber is related to its temperature, the specific energy of the gas is given by:

$$\begin{cases} e_q = c_p T_q, \\ e_i = \begin{cases} c_p T_p & p_p \geq p_q, \\ c_p T_q & p_p < p_q, \end{cases} \end{cases} \tag{16}$$

$$c_p = \frac{\gamma \cdot R}{\gamma - 1}. \tag{17}$$

After the projectile passes the front gas port, high-pressure propellant gas flows from the barrel into the front barrel clamp and gas-transfer tube. It then enters the central gas port of the rotating piston and is subsequently directed into the high-pressure chamber through the radial gas port. The mass flow rate of gas entering the high-pressure chamber is given by Eq. (18) [23].

$$q_{mb} = \begin{cases} \mu_b S_b K_0 \sqrt{p_b \rho_b}, & p_q \le \zeta p_b \,, \\ \mu_b S_b \sqrt{\dfrac{2\gamma}{\gamma-1} p_b \rho_b \left[\left(\dfrac{p_q}{p_b}\right)^{\frac{2}{\gamma}} - \left(\dfrac{p_q}{p_b}\right)^{\frac{\gamma+1}{\gamma}} \right]}, & \zeta p_b < p_q < p_b \,, \\ -\mu_b S_b \sqrt{\dfrac{2\gamma}{\gamma-1} p_q \rho_q \left[\left(\dfrac{p_b}{p_q}\right)^{\frac{2}{\gamma}} - \left(\dfrac{p_b}{p_q}\right)^{\frac{\gamma+1}{\gamma}} \right]}, & \zeta p_q < p_b < p_q \,, \\ -\mu_b S_b K_0 \sqrt{p_q \rho_q}, & p_b \le \zeta p_q \,. \end{cases} \tag{18}$$

Based on the previously stated assumption, gas leakage through the gap between the high-pressure chamber and the piston is treated as critical flow. The expression for the corresponding mass flow rate is given by:

$$q_{mq} = \mu_q \Delta S_b K_0 \sqrt{p_q \rho_q} \,. \tag{19}$$

After the propellant gas enters the high-pressure chamber, it drives the motion of the rotating piston. The motion of the rotating piston obeys Newton's second law, and its equation of motion is expressed as:

$$\begin{cases} J_h \dfrac{d\omega}{dt} = 3(p_q - p_a) l_1 (r_1 - r_2) r_h - T_f \,, \\ T_f = T_n + 3fN + T', \\ \dfrac{d\theta}{dt} = \omega, \end{cases} \tag{20}$$

where J_h is the rotational inertia of the rotating piston; r_h is the average effective radius at which the driving force acts on the end face of the piston lug; T_f is the resistance torque acting on the rotating piston; T_n is the torque exerted by the torsion spring on the one-way valve; T' is the frictional resistance torque between the rotating piston and the rear barrel clamp; N is the normal contact force between the piston lug and the one-way valve when the lug drives the valve; and f is the coefficient of friction.

When the rotating piston drives the exhaust rotor to rotate, the flow area between the rear exhaust port and the exhaust duct increases as the angle between their central axes decreases. The flow condition is shown in Fig. 6. Given that both the rear exhaust port and the exhaust duct have a radius of r, the exhaust rotor has

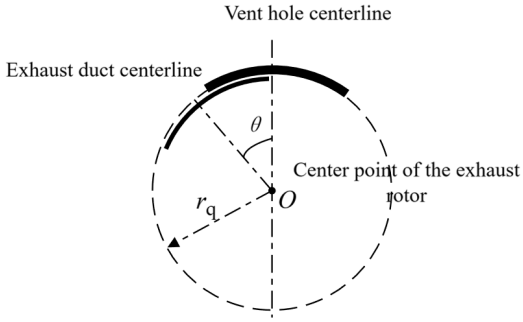


Fig. 6. Schematic of the exhaust passage and exhaust port alignment

a radius of r_q, and the angle between their central axes is θ_h, the flow area S_t is expressed as:

$$S_t = 2r^2 \arccos\left(\frac{r_q \sin(|\theta_h|/2)}{r}\right) - r_q \sin\left(\frac{|\theta_h|}{2}\right)\sqrt{4r^2 - 4r_q^2 \sin^2\left(\frac{|\theta_h|}{2}\right)}, \quad (21)$$

$$x_f = r_q \theta_h \,. \quad (22)$$

3.4. Mathematical model of the locking pin

After the projectile passes the rear exhaust port, a small amount of propellant gas enters the lateral gas channel from the bore. This gas overcomes the preload of the return spring and frictional resistance, driving the locking pin forward. Once the exhaust rotor rotates to the designated angular position, the locking pin engages the locking hole on the rotor, thereby precisely positioning the exhaust rotor. Owing to the relatively small volume and sealed nature of the lateral gas channel, the gas flow within it is modeled using a quasi-steady zero-dimensional approach. The motion of the locking pin is governed by Newton's second law [13, 23]:

$$\begin{cases} m_h \dfrac{dv_h}{dt} = A_h(p_k - p_a) - (F_0 + k_h \cdot x_h) - F_h \,, \\ \dfrac{dx_h}{dt} = v_h \,, \end{cases} \quad (23)$$

where v_h is the velocity of the locking pin, x_h is its displacement, m_h is the mass of the locking pin, A_h is the cross-sectional area of the lateral gas channel, p_k is the pressure inside the lateral gas channel, p_a is the ambient pressure, F_0 is the preload force of the locking-pin spring, k_h is the spring stiffness, and F_h represents the combined frictional resistance. When the in-bore pressure drops such that the spring force exceeds the pressure force in the lateral channel, the locking pin returns to its initial position. The governing equation for the reset motion is similar to Eq. (23).

3.5. Process of the solution method

The overall solution procedure is illustrated in Fig. 7. After primer ignition, the projectile is accelerated toward the muzzle by the propellant gas. Prior to the projectile passing the rear exhaust port, only the in-bore two-phase flow governing equations (Eqs. (1)–(7)) are solved, with the coupling terms $\boldsymbol{L}$, $\boldsymbol{J}$, and $\boldsymbol{K}$ set to zero. Once the projectile passes the rear exhaust port, the flow fields in the bore and the lateral gas channel become coupled, and the mass, momentum, and energy exchange between them is accounted for through the source term $\boldsymbol{L}$ in Eq. (1). Similarly, after the projectile passes the front gas port, the in-bore flow field is coupled with the gas-transfer tube and high-pressure chamber, with the corresponding interactions incorporated via the source term $\boldsymbol{J}$ in Eq. (1). When the high-pressure gas enters the rotary valve chamber through the gas-transfer tube, the gas-dynamic model described by Eqs. (8)–(22) is activated to simulate the motion of the rotary piston and exhaust rotor.

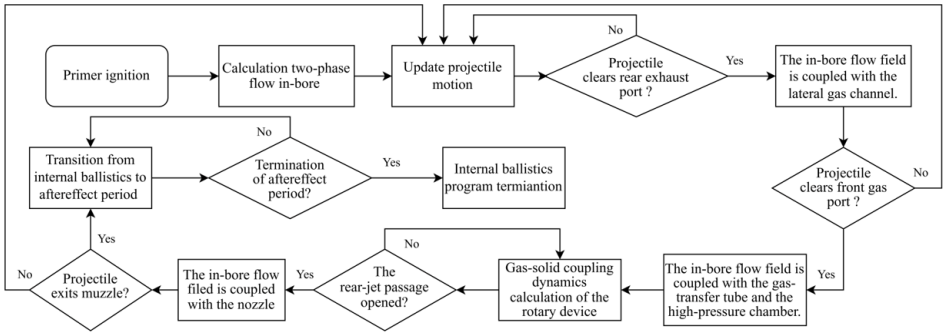


Fig. 7. Solution procedure

When the exhaust channel opens, the bore flow field becomes further coupled with the rear-jet nozzle flow, and the associated mass and momentum exchange is represented by the source term $\boldsymbol{K}$. At this stage, the locking pin engages the locking hole to achieve precise positioning of the exhaust rotor, while the flow parameters in the rear-jet nozzle are solved using the corresponding governing equations. After the projectile exits the muzzle and enters the aftereffect period, the fully coupled governing equations continue to be solved until the in-bore pressure drops to ambient level.

4. Numerical simulation solution and results analysis

4.1. Numerical solution methodology for the model

Numerical simulations were performed for a 14.5 mm three-barrel rotary barrel weapon. The governing equations in the bore and exhaust nozzle were solved using a second-order accurate MacCormack finite-difference scheme [25]. The

equations in the lateral gas channel were integrated using a second-order Runge–Kutta method [8], while those in the high-pressure chamber were solved with a fourth-order Runge–Kutta scheme. The time step was determined based on the CFL condition. When the rear-jet nozzle remained closed, the time-step size was governed by the CFL criterion in the in-bore domain [26]. Once the rear-jet nozzle opened, the minimum CFL value from both the in-bore and exhaust-nozzle domains was adopted to ensure numerical stability.

To verify the reliability of the two-phase interior ballistic model and the numerical implementation, the simulated results for the conventional rotary barrel weapon (without the recoil-reduction device) were compared with available data from the literature [27–29], as shown in Table 1. Fig. 8 shows the pressure-time curves for the reference data and the computed data. Good agreement was achieved between the present results and the reference data.

Table 1. Numerical results

Computed value	Acceptable range	Present
Maximum breech pressure [MPa]	315–350	340
Muzzle velocity [m·s^{-1}]	945–1005	960.42
Exit time [ms]	3.0–3.5	3.05

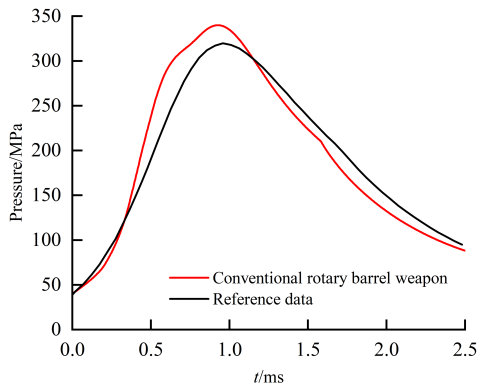


Fig. 8. Pressure comparison of calculation data and reference data

4.2. Analysis of pressure in the barrel

To evaluate the influence of the GRV rear-jet control device on weapon performance, a comparative analysis was conducted between the rotary barrel weapon equipped with the recoil-reduction device and the conventional baseline weapon. Due to the strong coupling between the in-bore flow field and the device flow field, these parameters are mutually constrained and nonlinear. It is difficult to solve this

relationship analytically. Reasonable parameter matching can be achieved through a large number of numerical calculations. With a muzzle velocity reduction limit of 1% imposed as the design constraint, appropriate system parameters were determined through extensive numerical simulations. The firing rate was set to 3000 rounds/min. The main structural parameters of the rotary barrel weapon are listed in Table 2. For devices with different structural dimensions or operating conditions, the parameters would need to be re-matched.

Table 2. Fundamental specifications

Parameters	Value	Parameters	Value
Caliber [mm]	14.5	Radius of the rotating piston [mm]	9.5
Barrel length [m]	1.26	Outer radius of the piston lug [mm]	14
Projectile mass [kg]	0.064	Radius of the average effective [mm]	11.75
Chamber volume [10^{-6}m^3]	37.7	Width of the piston lug [mm]	12
Propellant mass [g]	31	Initial volume of high-pressure chamber [10^{-7}m^3]	4.98
Propellant energy [J·kg^{-1}]	9.2e5	Rotational inertia of the rotating piston [g·m^2]	6.94e-3
Burning rate exponent of propellant [n]	0.83	Stiffness of the torsion spring [N·m/deg]	0.02
Propellant density [kg·m^{-3}]	1600	Radius of the exhaust rotor [mm]	11.5
Propellant half-thickness [mm]	0.264	Mass of the locking pin [kg]	6e-4
Adiabatic index	1.25	Stiffness of the locking pin spring [N·m^{-1}]	5000
Number of perforations	7	Pressure-bearing area of the locking pin [mm^2]	12.57
Distance from the rear exhaus port to the chamber base [mm]	360	Rear-jet length [m]	0.1
Distance from the front gas port to the chamber base [mm]	640	Expansion nozzle divergence angle [°]	24
Diameter of the rear exhaust port [mm]	12	Diameter of the radial gas port [mm]	2
Diameter of the front gas port [mm]	6	Ambient pressure [Pa]	1.01e5

To examine the sensitivity of the predicted performance to the rear-jet timing, the effect of the rear exhaust port position on the muzzle velocity, and recoil impulse is further investigated in Table 3.

As the rear exhaust port is moved from 0.31 to 0.41 m, the muzzle-velocity loss decreases from 1.42% to 0.65%, whereas the recoil-reduction efficiency decreases

Table 3. Sensitivity of the rear exhaust port position

Distance from the rear exhaust port to the chamber base [m]	Final recoil impulse [N·s]	Recoil reduction efficiency [%]	Muzzle velocity [m·s^{-1}]	Velocity loss [%]
0.31	52.76	49.82	946.75	1.42
0.335	54.16	48.49	948.33	1.26
0.36	55.88	46.85	952.29	0.85
0.385	57.43	45.38	953.36	0.74
0.41	58.48	44.39	954.20	0.65

from 49.82% to 44.39%. Because the distance decreases cause exhaust passage opening advance, thereby improving recoil reduction but producing a larger muzzle-velocity penalty. The positions of 0.31 and 0.335 m do not satisfy the prescribed muzzle-velocity-loss constraint of less than 1%. Among the feasible positions investigated, 0.36 m provides the highest recoil-reduction efficiency and is therefore selected as the nominal rear exhaust-port position.

Figs. 9 and 10 compare the breech pressure and projectile base/muzzle pressure histories, respectively, for the two configurations during the firing process. In Fig. 10, the pressure curve represents the projectile base pressure before the projectile exits the muzzle and transitions smoothly to the muzzle pressure after the projectile leaves the barrel. As shown in Figs. 9 and 10, during the firing process of the GRV-equipped rotary barrel weapon, the projectile base pressure reaches a maximum of 286.57 MPa at 1.58 ms, while the breech pressure peaks at 340.02 MPa at 1.46 ms. The projectile passes the rear exhaust port at 1.78 ms, by which time both the breech and projectile base pressures have already attained their peak values. After the projectile passes the rear exhaust port, a slight drop in

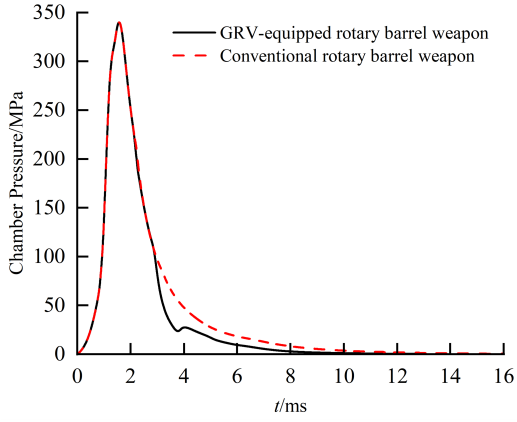


Fig. 9. Breech pressure comparison of two weapons

projectile base pressure occurs due to the diversion of a small amount of propellant gas into the lateral gas channel to drive the locking pin.

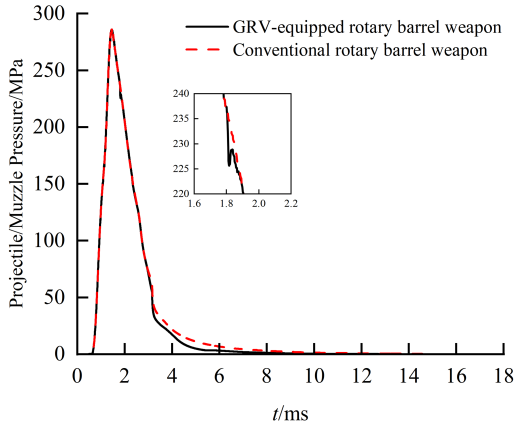


Fig. 10. Projectile/muzzle pressure comparison of two weapons

The rarefaction wave generated at the rear exhaust port reaches the breech at 2.84 ms and the projectile base at 3.16 ms. Prior to the arrival of this wave, the breech and projectile base pressure histories of the two weapons are nearly identical. Only after the rarefaction wave reaches the breech and projectile base do the pressures in the GRV-equipped weapon begin to deviate noticeably from those of the conventional weapon.

These results indicate that the discharge of propellant gas through the rear exhaust port does not cause an instantaneous pressure drop throughout the bore. Instead, the pressure reduction propagates as a rarefaction wave at a finite speed. The pressure decreases only in regions where the rarefaction wave has passed, while areas not yet reached by the wave maintain pressures identical to those in the conventional system. Therefore, proper consideration of the timing and propagation characteristics of the rarefaction wave is essential in the design to ensure effective rearward discharge of a large volume of propellant gas.

4.3. Analysis of flow field in the lateral gas channel

As shown in Figs. 11 and 12, at 1.78 ms after ignition, when the projectile reaches the rear exhaust port, a small amount of propellant gas immediately enters the lateral gas channel. Because the pressure in the bore is initially much higher than that in the lateral channel, the channel pressure and gas density increase rapidly, thereby driving the locking pin against the spring force. At 1.83 ms, the locking pin reaches its limiting position, and the pressure and gas density in the lateral gas channel attain their maximum values. As the projectile continues to travel forward, the pressure in the bore near the rear exhaust port decreases. Consequently, the

pressure difference between the bore and the lateral gas channel is reduced, which decreases the gas inflow rate into the channel. The pressure and gas density in the lateral gas channel therefore gradually decrease.

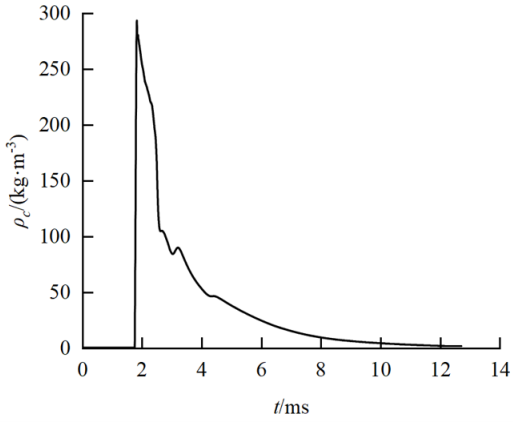


Fig. 11. Density-time curve in the lateral gas channel

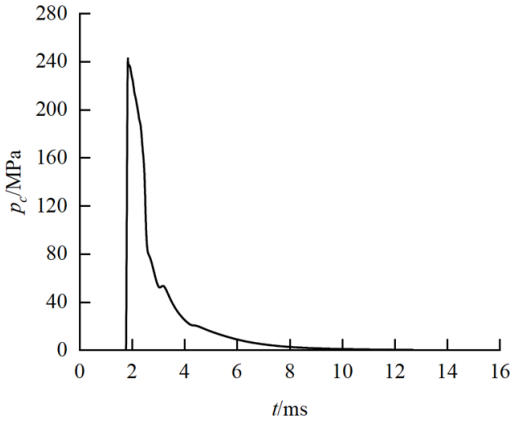


Fig. 12. Pressure-time curve in the lateral gas channel

Fig. 13 shows the displacement-time history of the locking pin in the lateral gas channel. Driven by the high-pressure propellant gas, the locking pin rapidly moves to its limit position and remains there for a period. After substantial propellant gas is discharged through the rear-jet nozzle, the locking pin returns to its initial position under the restoring force of the spring, reaching this position at approximately 12 ms. At a firing rate of 3000 rounds/min, the locking pin completes its reset before the next firing cycle begins, thereby avoiding any interference with subsequent firing operations.

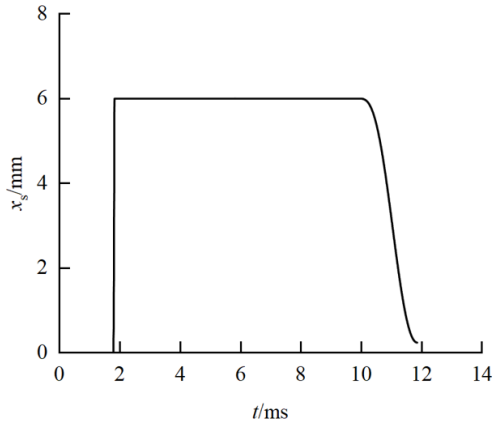


Fig. 13. Displacement-time history of the locking pin

4.4. Analysis of flow field in the barrel

To better characterize the evolution of propellant gas within the barrel and enable a direct comparison with the interior ballistic behavior of a conventional rotary barrel weapon, Figs. 14–16 present the axial distributions of chamber pressure, gas-phase velocity, and solid-phase velocity for the GRV system and the conventional system at different time instants.

In these figures, the breech is defined as the origin of the axial coordinate, with the muzzle direction taken as positive. The time origin corresponds to the instant of ignition. The curves in each figure represent the following characteristic stages of the firing process:
(1) before the projectile reaches the rear exhaust port (1.78 ms after ignition); (2) after the projectile passes the rear exhaust port but before reaching the front gas port (1.90 ms); (3) before the projectile reaches the front gas port (2.28 ms); (4) 0.07 ms after the front gas port opens, prior to the opening of the rear-jet passage (2.35 ms); (5) 0.03 ms after the rear-jet passage opens (2.49 ms); (6) 0.34 ms after the rear-jet passage is fully open (2.86 ms); (7) when the projectile reaches the muzzle (3.16 ms); (8) 1.22 ms after the projectile exits the muzzle (4.38 ms).

As shown in Figs. 14–16, before the projectile reaches the rear exhaust port at 1.78 ms, the in-bore flow-field parameters and projectile motion of the GRV-equipped rotary-barrel weapon are nearly identical to those of the conventional weapon. After the projectile clears the rear exhaust port, a small amount of propellant gas enters the lateral gas channel and drives the locking pin. Owing to the limited flow area and volume of this channel, the initial gas diversion produces only a minor and transient perturbation in the bore flow field. Accordingly, the profiles at 1.90 ms and 2.28 ms remain close to those of the conventional configuration.

In terms of pressure (Fig. 14), after the projectile clears the front gas port, propellant gas enters the gas-transfer path under the pressure difference between the

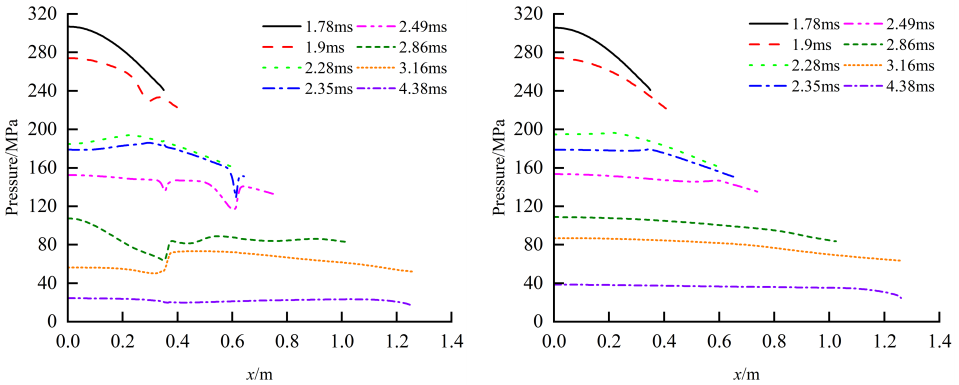


Fig. 14. Pressure curve. (a) GRV-equipped rotary barrel weapon; (b) Conventional rotary barrel weapon

bore and the gas-transfer tube. This gas diversion causes a local pressure reduction, as indicated by the 2.35 ms profile. Once the rear-jet passage begins to open, propellant gas is discharged from the bore into the rear-jet nozzle. The local pressure drop near the rear exhaust port becomes more pronounced at 2.49 ms and 2.86 ms. After the rear-jet passage is fully opened, the overall in-bore pressure decreases progressively. However, the pressure near the rear exhaust port remains lower than that in adjacent regions and lower than that of the conventional configuration at the same location. This behavior results from the rarefaction wave generated by gas discharge, which reduces the pressure in the regions through which it propagates. After projectile exit, propellant gas is discharged simultaneously from the muzzle and the rear-jet nozzle. The in-bore flow field gradually becomes smoother, and the pressure discontinuities are progressively attenuated and eventually disappear during the aftereffect period, as shown at 4.38 ms.

In terms of gas-phase velocity (Fig. 15), after the projectile clears the front gas port, propellant gas enters the GRV device because the in-bore pressure is higher than the pressure in the gas-transfer path and high-pressure chamber. This diversion causes a slight local decrease in gas-phase velocity. At 2.49 ms, a distinct velocity discontinuity develops on the two sides of the rear exhaust port. This discontinuity is associated with flow bifurcation after the rear-jet passage opens: an increasing amount of propellant gas is directed from the bore into the shared nozzle, producing a local pressure reduction near the rear exhaust port. Because the pressure at the rear exhaust port remains lower than that in adjacent regions, a local velocity-minimum region persists near the port. This enables a larger mass of propellant gas to be expelled rearward through the nozzle, producing a forward reaction impulse that effectively reduces the recoil impulse.

For solid-phase velocity (Fig. 16), the response of the propellant particles is influenced by the gas-phase flow, although it is weaker and delayed because of

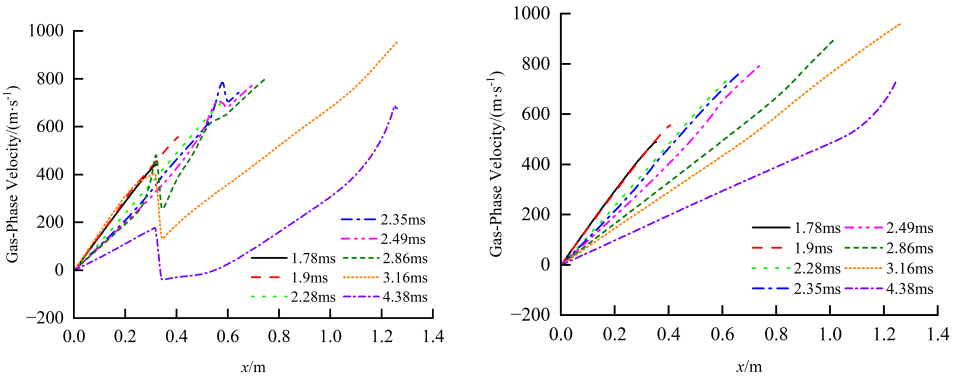


Fig. 15. Gas-phase velocity profile. (a) GRV-equipped rotary barrel weapon; (b) Conventional rotary barrel weapon

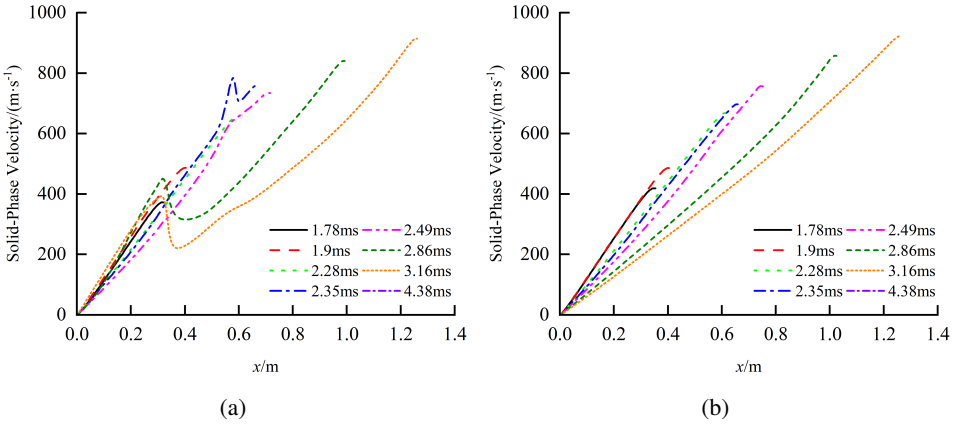


Fig. 16. Solid-phase velocity profile. (a) GRV-equipped rotary barrel weapon; (b) Conventional rotary barrel weapon

particle inertia. After the projectile clears the front gas port, the pressure difference between the bore and the gas-transfer path causes a slight local decrease in solid-phase velocity near the port, as shown by the 2.35 ms profile. Once the rear-jet passage opens, the rapid pressure reduction near the rear exhaust port produces a more pronounced local decrease in solid-phase velocity. However, particles that have already passed the local low-pressure region retain relatively high forward velocities because of their inertia. Meanwhile, particles closer to the breech continue to be accelerated by the surrounding high-pressure gas. Consequently, a region of relatively high solid-phase velocity remains closer to the breech than in the conventional configuration, as shown at 2.86 ms and 3.16 ms.

4.5. Analysis of projectile muzzle velocity

Figs. 17 and 18 show the projectile velocity-time and displacement-time histories, respectively, for the GRV-equipped weapon and the conventional rotary barrel weapon. As shown in Figs. 10 and 17, although a portion of the propellant gas is diverted for rearward ejection in the proposed system, the overall pressure impulse imparted to the projectile during its in-bore travel remains nearly identical to that of the conventional weapon. This indicates that the energy extracted by the recoil-reduction device has a negligible effect on the net work done on the projectile, resulting in only minor differences in the velocity-time profiles.

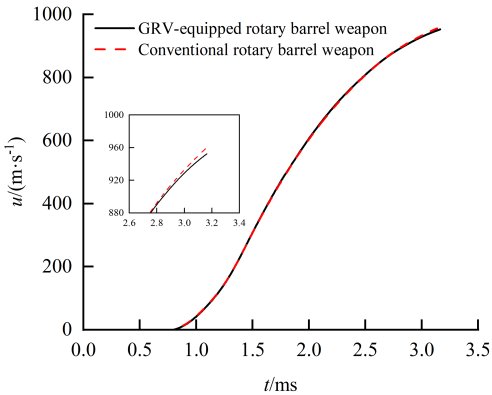


Fig. 17. Comparison of projectile velocity-time curves for two weapons

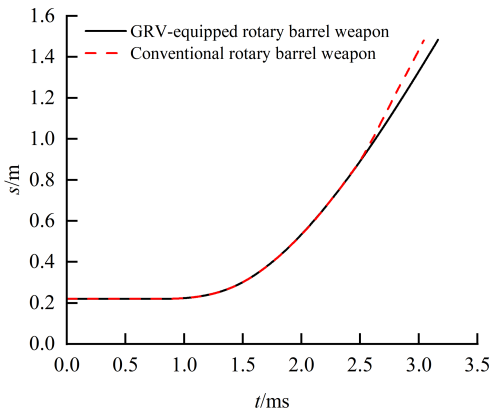


Fig. 18. Comparison of projectile displacement-time curves for two weapons

Once the projectile passes the front gas port, a small quantity of high-pressure propellant gas enters the gas-transfer tube and drives the rotary piston, which in turn rotates the exhaust rotor through the connecting rod. Owing to the limited

internal volume and the initially sealed state of the gas-transfer tube and rotary piston, the resulting pressure drop at the projectile base is minimal. Consequently, this reduction in projectile base pressure has only a slight effect on the projectile's in-bore acceleration.

As illustrated in Fig. 17, the muzzle velocity of the conventional rotary barrel weapon is 960.42 m/s, whereas that of the GRV-equipped rotary barrel weapon is 952.29 m/s, corresponding to a reduction of only 0.85%. This modest velocity loss is primarily attributed to the delayed activation of the gas-diversion process, which minimizes interference with the main acceleration phase of the projectile. Additionally, the interior ballistic duration of the gas-guided system is slightly extended, increasing from 3.05 ms to 3.16 ms (Fig. 18), indicating a marginally prolonged acceleration process due to gas extraction.

4.6. Analysis of the recoil reduction efficiency

The recoil-reduction efficiency analysis in this study focuses on the components rigidly connected to the barrel assembly, excluding the contributions of the muzzle brake, counter-recoil mechanism, or other buffering devices. The formulas for calculating the resultant force on the weapon system and the recoil impulse are given in Ref. [8]. The recoil-reduction efficiency η is defined as:

$$\eta = \frac{I_0 - I}{I_0} \times 100\%. \tag{24}$$

In Eq. (24), I_0 and I represent the recoil impulse of the conventional rotary barrel weapon and the GRV-equipped rotary barrel weapon, respectively. The forward direction of the projectile in the bore is taken as positive. Fig. 19 compares the axial resultant force acting on the gun body for the two weapons. Fig. 20 compares the recoil impulse histories of the two weapons, while Fig. 21 shows the

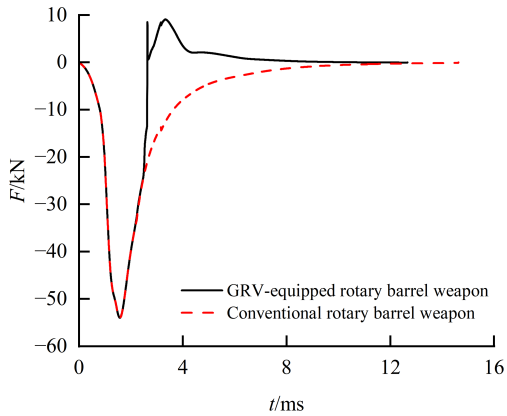


Fig. 19. Comparison of recoil for two weapons

time history of the total mass of propellant gas discharged through the rear exhaust port for the GRV-equipped rotary barrel weapon.

As shown in Fig. 10, at a firing rate of 3000 rounds/min, the total duration of the interior ballistic phase and aftereffect period for each shot is less than 20 ms, corresponding to one complete firing cycle. Therefore, the recoil-reduction device is capable of operating effectively within each firing cycle.

As illustrated in Fig. 19, the axial resultant force acting on the rotary barrel weapon equipped with the recoil-reduction device initially follows a similar trend to that of the conventional weapon. Compared with the conventional configuration, the axial resultant force of the GRV-equipped rotary barrel weapon begins to decrease slightly at 2.62 ms due to the initial rearward discharge of a small amount of propellant gas through the lateral channel. Subsequently, as a large volume of propellant gas is expelled through the rear-jet nozzle, a strong forward reaction thrust is generated. This causes the axial resultant force to decrease rapidly, change direction, and reach a peak reverse force of 8916.45 N at 3.06 ms. As propellant gas continues to be discharged, the axial resultant force gradually approaches zero.

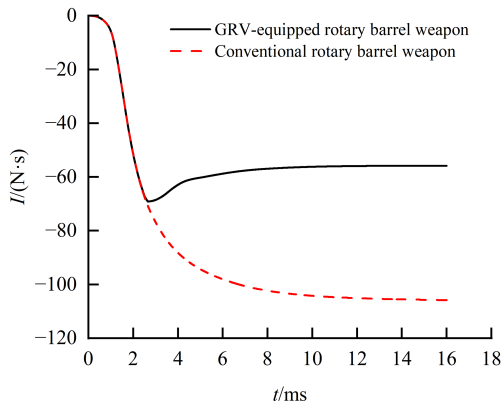


Fig. 20. Comparison of recoil momentum for two weapons

As shown in Fig. 20, the recoil impulse of the conventional rotary barrel weapon increases continuously due to accumulation during sustained firing. In contrast, the recoil impulse of the weapon equipped with the recoil-reduction device is significantly reduced by the rearward discharge of propellant gas. For the GRV configuration, the recoil impulse reaches a maximum of 71.03 N·s and eventually stabilizes at 55.88 N·s, compared with a final value of 105.14 N·s for the conventional weapon. Consequently, the proposed system achieves a recoil-reduction efficiency of 46.85%. The recoil reduction is produced by the rearward discharge of propellant gas through the shared nozzle. This discharge generates a forward reaction force on the weapon system, which offsets part of the rearward recoil force. In addition, diverting part of the propellant gas reduces the rearward

momentum carried by the gases discharged from the muzzle. The time integral of the net axial force determines the reduced recoil impulse.

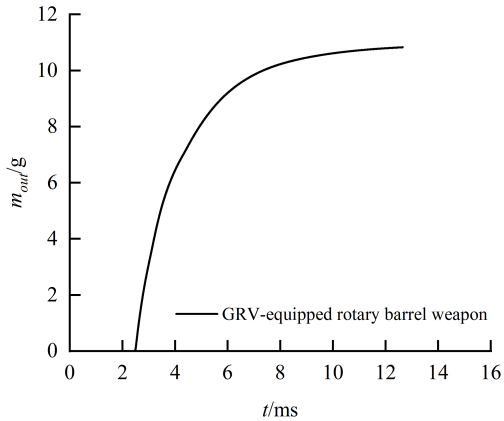


Fig. 21. Total mass of propellant gas discharged through the rear exhaust port

As shown in Fig. 21, the total mass of propellant gas discharged rearward through the rear exhaust port is 10.83 g. Compared with the previous piston-crankshaft scheme, the locking-pin positioning mechanism eliminates the oscillatory "drive–brake–reverse" behavior. This ensures that the exhaust port remains fully open throughout the discharge process, allowing a greater mass of propellant gas to be expelled rearward and thereby improving the overall recoil-reduction efficiency.

The present model evaluates the transient interior-ballistic, valve-dynamic, and recoil-reduction behavior of the proposed system, but it does not assess its structural durability or operational reliability during sustained high-rate firing. The periodic impact of propellant gas on the rotary valve, the fatigue loads acting on the springs, and the reliability concerns of the device under real operating conditions have not been quantified or discussed in the current analysis. Therefore, the actual recoil-reduction efficiency needs to be verified through subsequent experimental testing.

5. Conclusions

1. This study addresses the severe recoil accumulation issue in rotary barrel weapons during sustained firing. A novel recoil-reduction device based on a gas-guided rotary valve with a shared-nozzle rear-jet configuration is proposed. The device diverts propellant gases from the bore through a common rear-jet nozzle to generate a counteracting reaction force. While maintaining the projectile muzzle velocity essentially unchanged, the proposed system significantly reduces the recoil impulse of the weapon.

2. Based on a 14.5 mm three-barrel rotary barrel weapon, a gas-guided rotary valve shared-nozzle rear-jet device is designed, and its working principle as well as gas-guide strategy are described in detail. To investigate the influence of the proposed device on the in-bore flow characteristics, a one-dimensional two-phase flow model of the firing process is established. The governing equations are solved numerically using the MacCormack finite-difference scheme and the Runge–Kutta method. The evolution of the in-bore flow field at different time instants is analyzed.
3. Compared with a conventional rotary barrel weapon, the proposed system predicts a 46.85% reduction in recoil impulse at a firing rate of 3000 rds/min. The muzzle velocity decreases by 0.85% (from 960.42 m/s to 952.29 m/s). The total mass of propellant gas discharged rearward through the rear-jet nozzle reaches 10.83 g, indicating effective utilization of propellant energy. These numerical results indicate the potential of the proposed device to reduce recoil impulse while maintaining a small muzzle-velocity penalty under the present modeling conditions.
4. The key contribution of this study is the proposed gas-guided rotary-valve mechanism for coordinating rear-jet discharge from the firing barrel through a single shared nozzle. Under the selected nominal parameters and stated modeling assumptions, the coupled model indicates that this configuration has the potential to balance recoil reduction and muzzle-velocity preservation while reducing the complexity associated with separate recoil-mitigation devices for individual barrels. These findings provide a preliminary numerical basis for further development.

References

[1] Y.J. Song, H. Jeong, K.H. Kang, and K.S. Park. Input signal modeling for analysis of the gun firing vibration characteristics of Gatling gun. *Journal of Mechanical Science and Technology*, 39:6517–6526, 2025. doi: 10.1007/s12206-025-1002-y.

[2] K.J. Kang and H.I. Gimm. Numerical and experimental studies on the dynamic behaviors of a gun that uses the soft recoil system. *Journal of Mechanical Science and Technology*, 26:2167–2170, 2012. doi: 10.1007/s12206-012-0538-9.

[3] Q. Ouyang, J.J. Zheng, Z.C. Li, M. Hu, and J. Wang. Controllability analysis and testing of a novel magnetorheological absorber for field gun recoil mitigation. *Smart Materials and Structures*, 25:115041, 2016. doi: 10.1088/0964-1726/25/11/115041.

[4] M. Ahmadian and J.C. Poynor. An evaluation of magneto rheological dampers for controlling gun recoil dynamics. *Shock and Vibration*, 8:147–155, 2001. doi: 10.1155/2001/674830.

[5] J. Liu, G.J. Shen, Y.L. Shen, and H.Y. Ren. The parameter optimization design of buffer device for Gatling gun. *Journal of Gun Launch & Control*, 41(02):64–68, 2020. doi: 10.19323/j.issn.1673-6524.2020.02.013. (in Chinese)

[6] J.S. Li, M. Qiu, Z.Q. Liao, D.P. Xian, and J. Song. Dynamic modeling and simulation of Gatling gun with muzzle assistant-rotating and recoil absorber. *Acta Armamentarii*, 35(9):1344–1349, 2014. doi: 10.3969/j.issn.1000-1093.2014.09.003. (in Chinese)

[7] X.Y. Zhao and Y. Lu. Multi-objective optimization of a muzzle brake to enhance overall performance. *AIP Advances*, 13:085020, 2023. doi: 10.1063/5.0145731.

[8] M. Qiu, J. Song, and Z.Q. Liao. *New principles and new technologies of weapon for energy utilization of gunpowder gas*. National Defense Industry Press, Beijing, 2022. (in Chinese)

[9] Z.Q. Liao and M. Qiu. *Gas dynamics of automatic weapons*. National Defense Industry Press, Beijing, 2015. (in Chinese)

[10] H.Q. Li. *Study on the firing vibration and its control technology of certain vehicle Gatling gun with high firing frequency*. Ph.D. Thesis, Nanjing University of Science and Technology, Nanjing, China, 2014. (in Chinese)

[11] Z.B. Han. *Study on intermittent oscillation dynamics and recoil reduction mechanism of a piston-crankshaft rear-jet device for rotary barrel weapons*. Nanjing University of Science and Technology, Nanjing, China, 2025. (in Chinese)

[12] P. Si, M. Qiu, Z.Q. Liao, J. Song, and L.X. Ma. Numerical simulation of two-phase flow in a side spray gun considering piston reset motion. *Explosion and Shock Waves*, 41(8):084201, 2021. doi: 10.11883/bzycj-2020-0252. (in Chinese)

[13] M. Qiu, F. Guo, J. Song, and P. Si. Recoil reduction design of gas-controlled side-jet gun based on bifurcated two-phase flow model. *Journal of Mechanical Science and Technology*, 37:1845–1857, 2023. doi: 10.1007/s12206-023-0323-y.

[14] M.M. Rashad, X.B. Zhang, H.E. Sadek, and C. Cheng. Two-phase flow interior ballistics model of naval large caliber guided projectile gun system. *Applied Mechanics and Materials*, 465–466:592–6, 2013. doi: 10.4028/www.scientific.net/AMM.465-466.592.

[15] J. Nussbaum, P. Helluy, J.M. Hérard, and A. Carriére. Numerical simulations of gas-particle flows with combustion. *Flow, Turbulence and Combustion*, 76:403-417, 2006. doi: 10.1007/s10494-006-9028-4.

[16] C. Cheng and X.B. Zhang. Numerical investigation of two-phase reactive flow with two moving boundaries in a two-stage combustion system. *Applied Thermal Engineering*, 156:422–431, 2019. doi: 10.1016/j.applthermaleng.2019.04.061.

[17] J.S. Jang, S.H. Oh, and T.S. Roh. Development of three-dimensional numerical model for combustion-flow in interior ballistics. *Journal of Mechanical Science and Technology*, 30:1631–1637, 2016. doi: 10.1007/s12206-016-0319-y.

[18] X.L. Dong, X.T. Rui, C. Li, Y. Wang, and L.L. Fan. A calculation method of interior ballistic two-phase flow considering the recoil of gun barrel. *Applied Thermal Engineering*, 185:116239, 2021. doi: 10.1016/j.applthermaleng.2020.116239.

[19] L.H. Fu and W.J. Ruan. Analysis of recoilless cannon in one-dimensional two-phase flow. *Journal of Ordnance Equipment Engineering*, 40:51-55, 2019. doi: 10.11809/bqzbgcxb2019.07.011. (in Chinese)

[20] G. Monreal-González, R.A. Otón-Martínez, F.J.S. Velasco, and F.J. Ramírez-Fernández. One-dimensional modelling of internal ballistics. *Journal of Energetic Materials*, 35(4):397–420, 2017. doi: 10.1080/07370652.2016.1265613.

[21] I.S. Menshov, M.Y. Nemtsev, and I.V. Semenov. Numerical modeling of wave processes accompanying combustion of inhomogeneously distributed composite propellant. *Computational Mathematics and Mathematical Physics*, 59:1528–1541, 2019. doi: 10.1134/S0965542519090148.

[22] M. Qiu, P. Si, J. Song, and Z.Q. Liao. Recoil reduction method of gun with side to rear jet controlled by piston motion. *Symmetry*, 13(3):396, 2021. doi: 10.3390/sym13030396.

[23] W. Lv, M. Qiu, Y.S. Xu, and Y.X. Tao. Flow characteristics and pressure differential regulation in certain dual-chamber systems with the vent-hole gas control. *Aerospace Science and Technology*, 168:111091, 2026. doi: 10.1016/j.ast.2025.111091.

[24] S.S. Chen, R.Y. Tao, X.T. Cui, and S. Xue. Multi-parameter conflict mechanism and evaluation criteria of combustible ignition tube based on two-phase flow method. *Measurement*, 249:116953, 2025. doi: 10.1016/j.measurement.2025.116953.

[25] C.B. Hu and X.B. Zhang. A Riemann problem based coupling method for predicting the combustion of propellant in a gun launching process. *Propellants, Explosives, Pyrotechnics*, 44(6):751–758, 2019. doi: 10.1002/prep.201800293.

[26] C.S. Weng and H. Wang. *Computational interior ballistics*, National Defense Industry Press, Beijing, 2006. (in Chinese)

[27] F. Zhang, Z.Q. Liao, G.X. Liu, and Y. Chen. Interior ballistic research on reversely jet low recoil weapon. *Journal of Gun Launch & Control*, 110(02):6–10, 2008. doi: 10.19323/j.issn.1673-6524.2008.02.002. (in Chinese)

[28] Z.Y. Huang, Y.J. Jia, P.T. Cui, and J.F. Fan. Modulating technology for combustion performance of azidonitramine gun propellant. *Chinese Journal of Energetic Materials*, 21(6):795–799, 2013. doi: 10.3969/j.issn.1006-9941.2013.06.021. (in Chinese)

[29] S. Pavlovich. A discussion of observable characteristics and design features for the workshop manufactured Zagros 12.7×108 mm calibre and Zagros Şer 14.5×114 mm calibre anti-materiel rifles in use by Kurdish militia forces in northern Syria. *AFTE Journal*, 51:92–107, 2019.